


 Cite this: *RSC Adv.*, 2021, **11**, 16841

# Hydrodynamic synthesis of $\text{Fe}_2\text{O}_3@\text{MoS}_2$ 0D/2D-nanocomposite material and its application as a catalyst in the glycolysis of polyethylene terephthalate<sup>†</sup>

Younghyun Cha, Yong-Ju Park and Do Hyun Kim \*

We report a fast and simple synthesis of  $\text{Fe}_2\text{O}_3@\text{MoS}_2$  0D/2D-nanocomposite material using a Taylor-Couette flow reactor. A Taylor-Couette flow with high shear stress and mixing characteristics was used for fluid dynamic exfoliation of  $\text{MoS}_2$  and deposition of uniform  $\text{Fe}_2\text{O}_3$  nanoparticles, resulting in a  $\text{Fe}_2\text{O}_3@\text{MoS}_2$  in the form of 0D/2D-nanocomposite material. Using Taylor-Couette flow reactor, we could synthesize  $\text{Fe}_2\text{O}_3@\text{MoS}_2$  0D/2D-nanocomposite material at a rate higher than 1000 mg h<sup>-1</sup> which is much higher than previously reported production rate of 0.2–116.7 mg h<sup>-1</sup>. The synthesis of  $\text{Fe}_2\text{O}_3@\text{MoS}_2$  nanocomposite was achieved in an aqueous solution without thermal or organic solvent treatment. Exfoliated  $\text{MoS}_2$  nanosheets show an average thickness of  $2.6 \pm 2.3$  nm (<6 layers) and a lateral size of  $490 \pm 494$  nm.  $\text{Fe}_2\text{O}_3$  nanoparticles have an average size of  $7.4 \pm 3.0$  nm.  $\text{Fe}_2\text{O}_3$  nanoparticles on chemically and thermally stable  $\text{MoS}_2$  nanosheets show catalytic activity in the glycolysis of polyethylene terephthalate (PET). High conversion of PET (97%) and a high yield (90%) for bis(hydroxyethyl) terephthalate (BHET) were achieved in a reaction time of 3 h at the reaction temperature of 225 °C.

 Received 24th March 2021  
 Accepted 24th April 2021

 DOI: 10.1039/d1ra02335g  
[rsc.li/rsc-advances](http://rsc.li/rsc-advances)

## Introduction

Two-dimensional (2D) nanosheets such as graphene, transition metal dichalcogenides (TMD), and hexagonal boron nitride (hBN) may be promising for heterogeneous catalyst supports<sup>1–3</sup> because of their outstanding mechanical strength<sup>4</sup> and high surface area.<sup>5</sup> Among 2D layered materials,  $\text{MoS}_2$  nanosheets exhibit thermal and chemical stability,<sup>6–8</sup> and antioxidation properties<sup>9</sup> and thus were used as 2D substrates for the 0D/2D-nanocomposite material with noble metal<sup>10,11</sup> and metal oxide.<sup>12</sup> Among these, the combination of  $\text{MoS}_2$  nanosheets with iron oxide nanoparticles enhanced electrochemical, optical, and catalytic properties by chemical bonding-induced synergistic effect such as heterojunction on the 0D/2D-nanomaterial platform.<sup>13–15</sup> To synthesize iron oxide nanoparticles and  $\text{MoS}_2$

nanosheets composites, various methods have been reported.<sup>13–21</sup> Hydrothermal method is the most common method to synthesize either iron oxide nanoparticles or their composite with  $\text{MoS}_2$  nanosheets.<sup>13–17</sup> It can synthesize uniform iron oxide nanoparticles on the  $\text{MoS}_2$  nanosheets but it requires high temperature and pressure with long reaction time and has limited scale-up capacity due to energy inefficiency. Organic phase synthesis is similar to hydrothermal method, and it needs heating under inert gas conditions with organic solvents.<sup>18–20</sup> Most of previous methods have needed heat treatment, organic solvents, or specific conditions such as inert gas in the synthesis of iron oxide nanoparticles on the  $\text{MoS}_2$  nanosheets which hinder mass production and further applications.

Fluid dynamic system is one of the promising alternatives for mass-production of 0D/2D nanocomposite. Thus, synthesis of nanoparticles,<sup>22</sup> growth of polymers,<sup>23</sup> and exfoliation of 2D materials<sup>24,25</sup> were achieved using fluid dynamic system. Among the fluid dynamic systems, Taylor-Couette flow reactor with high shear stress and mass transfer characteristics was used for the exfoliation of 2D materials such as graphite, hBN, and  $\text{MoS}_2$ .<sup>24–26</sup> Our group reported deposition of noble metal (Pt, Ag, and Pd) nanoparticles on exfoliated hBN nanosheets in a Taylor-Couette flow reactor.<sup>27</sup> High shear stress and mixing characteristics of Taylor-Couette flow reactor allowed the

Department of Chemical & Biomolecular Engineering, KAIST, Daehak-ro 291, Yuseong-gu, Daejeon, 34141, Republic of Korea. E-mail: dohyun.kim@kaist.edu; Tel: +82-42-350-3929

† Electronic supplementary information (ESI) available: Dimension of the Taylor-Couette flow reactor, AFM image of  $\text{MoS}_2$  nanosheets, BET surface area of pristine  $\text{MoS}_2$ ,  $\text{MoS}_2$  nanosheets, and  $\text{Fe}_2\text{O}_3@\text{MoS}_2$  nanocomposite, TEM image of  $\text{Fe}_2\text{O}_3@\text{MoS}_2$  nanocomposite with different initial Fe : Mo ratio, TGA for  $\text{Fe}_2\text{O}_3@\text{MoS}_2$  nanocomposite, HPLC data for glycolysis of PET, recovered  $\text{Fe}_2\text{O}_3@\text{MoS}_2$  nanocomposite, comparison table for production of  $\text{Fe}_2\text{O}_3@\text{MoS}_2$  nanocomposite and previous reports, ICP-OES for  $\text{Fe}_2\text{O}_3@\text{MoS}_2$  nanocomposite, and BHET, comparison table for glycolysis reaction using  $\text{Fe}_2\text{O}_3@\text{MoS}_2$  nanocomposite and previous reports. See DOI: 10.1039/d1ra02335g



operation under mild reaction conditions in short reaction time.

Polyethylene terephthalate, commonly called PET, is one of the most consumed polymers in more than 300 million tons annually due to its mechanical strength and thermoplastic-based property.<sup>28,29</sup> Enormous consumption of PET in a daily life causes serious environmental problems due to poor biodegradability of PET.<sup>30,31</sup> To solve the problem, the chemical recycling methods such as alcoholysis,<sup>32</sup> aminolysis,<sup>33</sup> hydrolysis,<sup>34</sup> and glycolysis<sup>35</sup> were investigated. Among these, glycolysis of PET decomposes PET using ethylene glycol (EG) to produce bis(2-hydroxyethyl) terephthalate (BHET) monomers which can be used to synthesize polymers again providing the sustainability in the polymer ecosystem. The major drawback of PET glycolysis is slow reaction despite high temperature.<sup>36</sup> Heavy metal salts, known as trans-esterification catalysts, were used as catalysts for PET glycolysis to solve the problem.<sup>37,38</sup> Although the reaction temperature was lowered to around 200 °C, there was still an environmental problem due to the presence of heavy metals in recycled BHET monomers. To replace heavy metal salts, eco-friendly ionic liquids were used in PET glycolysis but their high cost was a concern.<sup>39,40</sup> Because of environmentally abundant and eco-friendly characteristics,<sup>35,41,42</sup> the use of cobalt oxide,<sup>43</sup> iron oxide,<sup>44</sup> and manganese oxide<sup>45</sup> was reported in the glycolysis of PET. However, needs for organic solvent-based processes and calcination make the synthetic processes of oxide material still formidable. Therefore, large-scale manufacturing of an effective catalyst material for PET recycling should be practiced in a more economical and eco-friendly routes.

Here, we report a fast and simple hydrodynamic synthesis method without heating for the synthesis of Fe<sub>2</sub>O<sub>3</sub> nanoparticles on exfoliated MoS<sub>2</sub> nanosheets in the form of 0D/2D-nanocomposites in a Taylor-Couette flow reactor. To the best of our knowledge, synthesis of Fe<sub>2</sub>O<sub>3</sub>@MoS<sub>2</sub> 0D/2D nanocomposites without heating or organic solvents has not been reported. The synthesis of Fe<sub>2</sub>O<sub>3</sub>@MoS<sub>2</sub> nanocomposite was achieved in an hour without organic solvents. Fe<sub>2</sub>O<sub>3</sub> nanoparticle is preferable for a catalyst because it is the most stable among iron oxides. However, it usually needs additional treatment such as calcination to convert Fe<sub>2</sub>O<sub>3</sub> from Fe<sub>3</sub>O<sub>4</sub>. Fluid dynamic process enabled the direct synthesis of Fe<sub>2</sub>O<sub>3</sub> nanoparticles on MoS<sub>2</sub> nanosheets. The synthetic Fe<sub>2</sub>O<sub>3</sub>@MoS<sub>2</sub> nanocomposite was used to validate its catalytic activity in PET glycolysis.

## Experimental procedure

### Materials and chemicals

Iron(III) chloride hexahydrate powder (FeCl<sub>3</sub>·6H<sub>2</sub>O, 99%), molybdenum disulfide powder (MoS<sub>2</sub>, <2 μm), sodium hydroxide (NaOH) powder, ethylene glycol (EG, 99.8%), and bis(2-hydroxyethyl) terephthalate (BHET) powder were purchased from Sigma-Aldrich Corporation (USA). Polyethylene terephthalate powder (PET, <200 μm, weight average molecular weight: 56 780 g mol<sup>-1</sup>) was obtained from Goodfellow Corporation (UK).

### Preparation of Fe<sub>2</sub>O<sub>3</sub>@MoS<sub>2</sub> nanocomposite

The schematic for the synthesis of Fe<sub>2</sub>O<sub>3</sub>@MoS<sub>2</sub> nanocomposite using the Taylor-Couette flow reactor is illustrated in Fig. 1a. Pristine MoS<sub>2</sub> powder (1000 mg) was initially dispersed in deionized (DI) water at a concentration of 2 mg mL<sup>-1</sup> in a 500 mL volume. Next, FeCl<sub>3</sub> powder (181 mg–3940 mg) was dispersed in MoS<sub>2</sub> aqueous mixture at various Fe : Mo molar ratio from 1 : 9 to 7 : 3. The MoS<sub>2</sub>/FeCl<sub>3</sub> mixtures were reacted for 1 h in the Taylor-Couette flow reactor with 2000 rotations per minute (rpm) of inner cylinder under room temperature. At the end of the reaction, 10 mL of 1 M NaOH aqueous solution was added to the Taylor-Couette flow reactor and reacted for 5 more minutes to convert FeCl<sub>3</sub> to Fe<sub>2</sub>O<sub>3</sub> nanoparticles. To compare the effect of mass transfer in the size distribution of Fe<sub>2</sub>O<sub>3</sub> nanoparticles, 3 different Fe<sub>2</sub>O<sub>3</sub>@MoS<sub>2</sub> nanocomposites with Fe : Mo molar ratio of 3 : 7 were synthesized at 3 different rotation speeds (500, 1500 and 2000 rpm) of inner cylinder in the Taylor-Couette flow reactor. Fe<sub>2</sub>O<sub>3</sub>@MoS<sub>2</sub> nanocomposite dispersed in the solution is shown in Fig. 1b. Synthetic Fe<sub>2</sub>O<sub>3</sub>@MoS<sub>2</sub> nanocomposite was centrifuged at 3200g for 1 h and separated from un-exfoliated MoS<sub>2</sub> followed by vacuum filtration using a cellulose nitrate filter (pore size: 100 nm) to extract extra ions (Na<sup>+</sup> and Cl<sup>-</sup>) from the supernatant. The filtered Fe<sub>2</sub>O<sub>3</sub>@MoS<sub>2</sub> nanocomposite was re-dispersed in 200 mL DI water and freeze-dried at –50 °C with 20 Pa to obtain Fe<sub>2</sub>O<sub>3</sub>@MoS<sub>2</sub> nanocomposite powder at a rate higher than 1000 mg h<sup>-1</sup> as shown in Fig. 1c. Detailed specification of the Taylor-Couette reactor was denoted in Fig. S1.<sup>†</sup>

### Characterization

The spherical aberration transmission electron microscopy (Cs-TEM) images were obtained by Titan3<sup>TM</sup> G2 60-300 (FEI). Transmission electron microscopy (TEM), scanning transmission electron microscopy (STEM), fast Fourier transform (FFT) diffraction pattern, and energy-dispersive X-ray spectroscopy (EDS) analysis were carried out by Tecnai G<sup>2</sup> F30 S-TWIN (FEI) operating at 300 kV. Raman spectroscopy data were obtained using LabRAM HR Evolution Visible\_NIR (HORIBA Co). Atomic force microscopy (AFM) data were obtained with

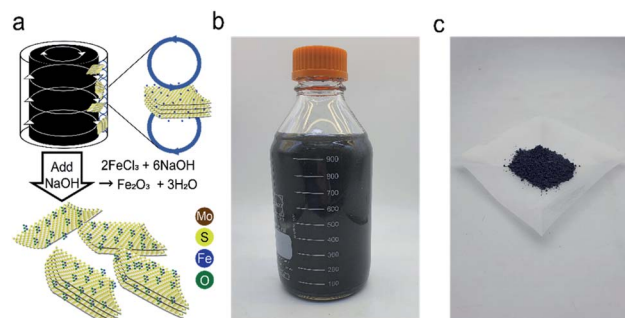


Fig. 1 (a) Schematic illustrations of the synthesis process of Fe<sub>2</sub>O<sub>3</sub>@MoS<sub>2</sub> nanocomposite by fluid dynamic exfoliation and deposition, (b) produced Fe<sub>2</sub>O<sub>3</sub>@MoS<sub>2</sub> nanocomposite in solution, (c) Fe<sub>2</sub>O<sub>3</sub>@MoS<sub>2</sub> nanocomposite powder.



INNOVA-LABRAM HR800 (Bruker Daltonik Co). X-ray photoelectron spectroscopy (XPS) data were acquired with a  $K\alpha$  (Thermo VG Scientific Co). Inductively coupled plasma-optical emission spectrometry (ICP-OES) analysis was carried out by Agilent ICP-OES 720 (Agilent Technologies). High performance liquid chromatography (HPLC) data were obtained by micrOTOF-QII (Bruker Daltonik Co) at 200–1000 parts per million (ppm) concentration in tetra hydro furan (THF). The thermogravimetric analysis (TGA)-differential scanning calorimetry (DSC) curves were obtained by LABSYS Evo (Setaram Co). Brunauer–Emmett–Teller (BET) analysis was carried out with Tristar II 3020 (Micromeritics Company). The  $^1\text{H}$  and  $^{13}\text{C}$  nuclear magnetic resonance (NMR) spectra analyses were carried out with Agilent 400 MHz 54 mm NMR DD2 (Agilent Technologies) at room temperature. The chemical shifts were denoted in ppm using dimethyl sulfoxide- $d_6$  (DMSO- $d_6$ ) signal as a standard.

### Glycolysis of PET

The condition for the glycolysis of PET was based on a previous report using iron oxide as a catalyst.<sup>44</sup> Prepared  $\text{Fe}_2\text{O}_3@\text{MoS}_2$  nanocomposite (20 mg) was dispersed in 8 g of EG, and the mixture was placed in a Teflon reactor along with 2 g of PET powder (Goodfellow, <200  $\mu\text{m}$ ). The reactants in the Teflon reactor were heated in a furnace between 200 and 300  $^\circ\text{C}$  for 3 to 5 h to examine the effect of temperature and time on glycolysis. Reacted solution was cooled to 70  $^\circ\text{C}$  in an oven. Vacuum filtration was performed to separate unreacted PET and catalyst from the product. The filtered solution was cooled in a refrigerator at 4  $^\circ\text{C}$  for 24 h. BHET was filtered by vacuum filtration followed by washing with cool DI water 3 times to remove extra EG. Mass of BHET was calculated by conventional HPLC

method with a calibration curve in the range of 200 to 1000 ppm.

Conversion of PET and the yield of BHET were calculated using eqn (1) and (2):<sup>27</sup>

$$\text{Conversion of PET}(\%) = 100 \times \frac{W_{\text{PET}} - W}{W_{\text{PET}}} (\%) \quad (1)$$

$$\text{Yield of BHET}(\%) = 100 \times \frac{W_{\text{BHET}} \div M_{\text{BHET}}}{W_{\text{PET}} \div M_{\text{PET}}} (\%) \quad (2)$$

In the equations above,  $W_{\text{PET}}$  represents the initial weight of PET, and  $W$  is the weight of PET after reaction.  $M_{\text{PET}}$  is the molecular weight of the repeated unit of PET.  $W_{\text{BHET}}$  is the weight of BHET based on the HPLC calibration curve, and  $M_{\text{BHET}}$  is the molecular weight of BHET.  $\text{Fe}_2\text{O}_3@\text{MoS}_2$  nanocomposite was recovered by vacuum filtration method. Due to more than 97% conversion of PET, the filtered precipitate was used for recycling as a recovered catalyst.

## Results and discussion

### Morphology of $\text{Fe}_2\text{O}_3@\text{MoS}_2$ nanocomposite

Morphology and crystalline structure of  $\text{MoS}_2$  nanosheets were investigated using AFM and TEM. AFM image of  $\text{MoS}_2$  nanosheets is presented in Fig. 2a. AFM data of 70 samples of  $\text{Fe}_2\text{O}_3@\text{MoS}_2$  nanocomposite were used to determine the average thickness and average lateral size (Fig. S2†).  $\text{MoS}_2$  nanosheets had an average lateral size of  $493.19 \pm 494.50$  nm and an average thickness of  $2.65 \pm 2.38$  nm, indicating successful exfoliation of  $\text{MoS}_2$  (Fig. 2b and c). Cs-TEM and EDS analysis were performed to confirm the deposition of  $\text{Fe}_2\text{O}_3$  nanoparticles on  $\text{MoS}_2$  nanosheets. Fig. 2d is the Cs-TEM image of

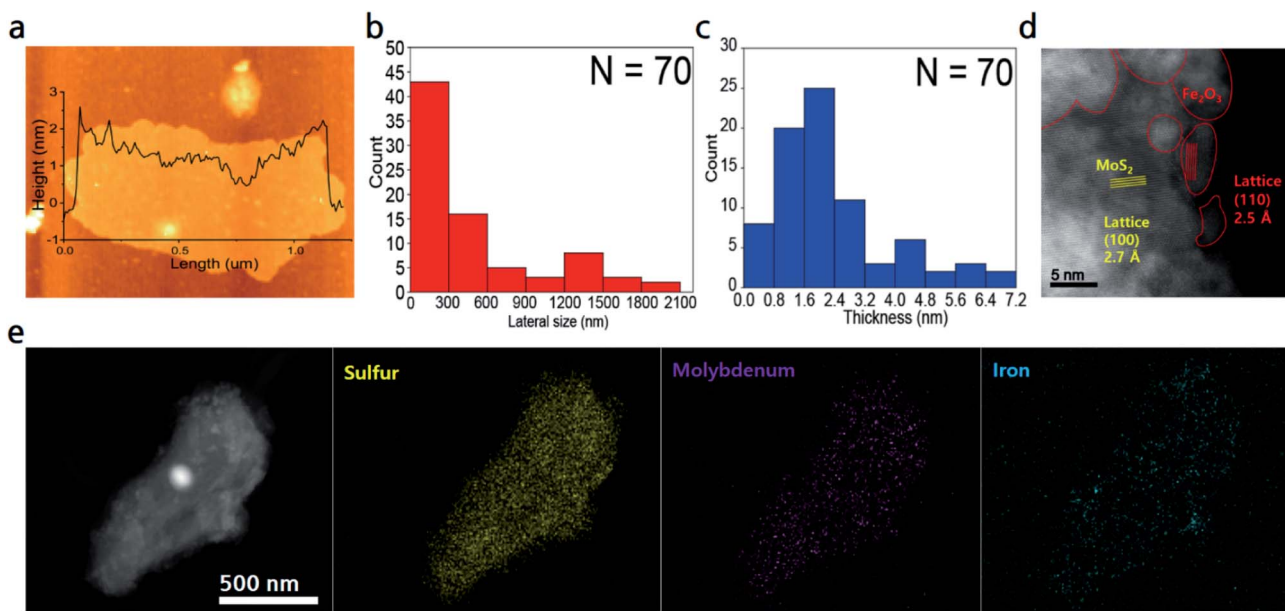


Fig. 2 (a) AFM image of  $\text{Fe}_2\text{O}_3@\text{MoS}_2$  nanocomposite. (b) Lateral size and (c) thickness distribution of  $\text{Fe}_2\text{O}_3@\text{MoS}_2$  nanocomposite. (d) Cs-TEM image of  $\text{Fe}_2\text{O}_3@\text{MoS}_2$  nanocomposite. (e) STEM image and elemental mapping images of sulfur, molybdenum, and iron of  $\text{Fe}_2\text{O}_3@\text{MoS}_2$  nanocomposite.



$\text{Fe}_2\text{O}_3@\text{MoS}_2$  nanocomposite. Specific lattice structures of iron oxide(III), denoted by red lines, were distinguished from the hexagonal lattice of the surrounding  $\text{MoS}_2$ . The characteristic lattice lengths of  $\text{Fe}_2\text{O}_3$  and  $\text{MoS}_2$  were 2.5 Å for (110) and 2.7 Å for (100), respectively.<sup>14</sup> EDS analysis of the same sample was performed to confirm the deposition of  $\text{Fe}_2\text{O}_3$  nanoparticles on the  $\text{MoS}_2$  nanosheet (Fig. 2e). The yellow signal of sulfur and the purple signal of molybdenum indicate  $\text{MoS}_2$  in the STEM image. The blue signal of Fe on the  $\text{MoS}_2$  indicates successful synthesis of  $\text{Fe}_2\text{O}_3@\text{MoS}_2$  nanocomposite.

BET surface area analysis was performed to further investigate the surface area of  $\text{Fe}_2\text{O}_3@\text{MoS}_2$  nanocomposite. Fig. S3† shows the BET surface area data of pristine  $\text{MoS}_2$ ,  $\text{MoS}_2$  nanosheets, and  $\text{Fe}_2\text{O}_3@\text{MoS}_2$  nanocomposite. In Fig. S3a, c and e,† BET surface area data show typical isotherm for 2D materials. The surface area of pristine  $\text{MoS}_2$  and  $\text{MoS}_2$  nanosheets was  $3.18 \text{ m}^2 \text{ g}^{-1}$  and  $9.33 \text{ m}^2 \text{ g}^{-1}$ , respectively in Fig. S3b and d.†  $\text{Fe}_2\text{O}_3@\text{MoS}_2$  nanocomposite had a surface area of  $47.95 \text{ m}^2 \text{ g}^{-1}$  and a higher slope isotherm due to  $\text{Fe}_2\text{O}_3$  nanoparticles (Fig. S3f†) which are consistent with previous reports despite being a top-down method.<sup>44</sup> Since it is a 0D/2D hybrid material, the surface area per unit mass is smaller than that of  $\text{Fe}_2\text{O}_3$  nanoparticles. Even with a less surface area,  $\text{MoS}_2$  nanosheets represent a stable substrate to prevent aggregation of  $\text{Fe}_2\text{O}_3$  nanoparticles and its lateral size facilitates the recovery of  $\text{Fe}_2\text{O}_3@\text{MoS}_2$  nanocomposite after reaction.

### Size distribution of $\text{Fe}_2\text{O}_3$ nanoparticles depending on flow regime in the Taylor–Couette flow reactor

TEM analysis was used to compare the distribution of  $\text{Fe}_2\text{O}_3$  nanoparticles in  $\text{Fe}_2\text{O}_3@\text{MoS}_2$  nanocomposite synthesized at various Fe : Mo ratios from 1 : 9 to 7 : 3. Fig. S4a and b† show  $\text{Fe}_2\text{O}_3@\text{MoS}_2$  nanocomposite synthesized with Fe : Mo ratio of 1 : 9.  $\text{Fe}_2\text{O}_3$  nanoparticles are rare on  $\text{MoS}_2$  nanosheets in high resolution image.  $\text{Fe}_2\text{O}_3@\text{MoS}_2$  nanocomposite synthesized with Fe : Mo ratio of 3 : 7 shows relatively more  $\text{Fe}_2\text{O}_3$  nanoparticles on  $\text{MoS}_2$  nanosheets in Fig. S4c and d.† The  $\text{Fe}_2\text{O}_3@\text{MoS}_2$  nanocomposite with Fe : Mo ratio of 5 : 5 shows fairly dense  $\text{Fe}_2\text{O}_3$  nanoparticles on  $\text{MoS}_2$  nanosheets (Fig. S4e and f†). For  $\text{Fe}_2\text{O}_3@\text{MoS}_2$  nanocomposite with Fe : Mo ratio of 7 : 3,  $\text{Fe}_2\text{O}_3$  nanoparticles are distributed more densely on  $\text{MoS}_2$  nanosheets than that with Fe : Mo ratio of 5 : 5 (Fig. S4g and h†). As expected, amount of  $\text{Fe}_2\text{O}_3$  nanoparticles on  $\text{MoS}_2$  nanosheets increased as ratio of Fe increased.

TEM images and FFT diffraction patterns of  $\text{Fe}_2\text{O}_3@\text{MoS}_2$  nanocomposite synthesized at different rotation speeds of inner cylinder in the Taylor–Couette flow reactor are shown in Fig. 3.  $\text{Fe}_2\text{O}_3$  nanoparticles are distributed well on  $\text{MoS}_2$  nanosheets with the characteristic hexagonal FFT diffraction patterns marked with yellow circles. Flow regimes in the Taylor–Couette flow reactor varied depending on rotation speed of inner cylinder as laminar, wavy, and turbulent regimes in the order of increasing rotation speed. Previously, our group reported efficiency of exfoliation for 2D materials in various flow regimes of Taylor–Couette flow and found about 2000 rpm corresponding to wavy regime is optimum for the exfoliation of 2D

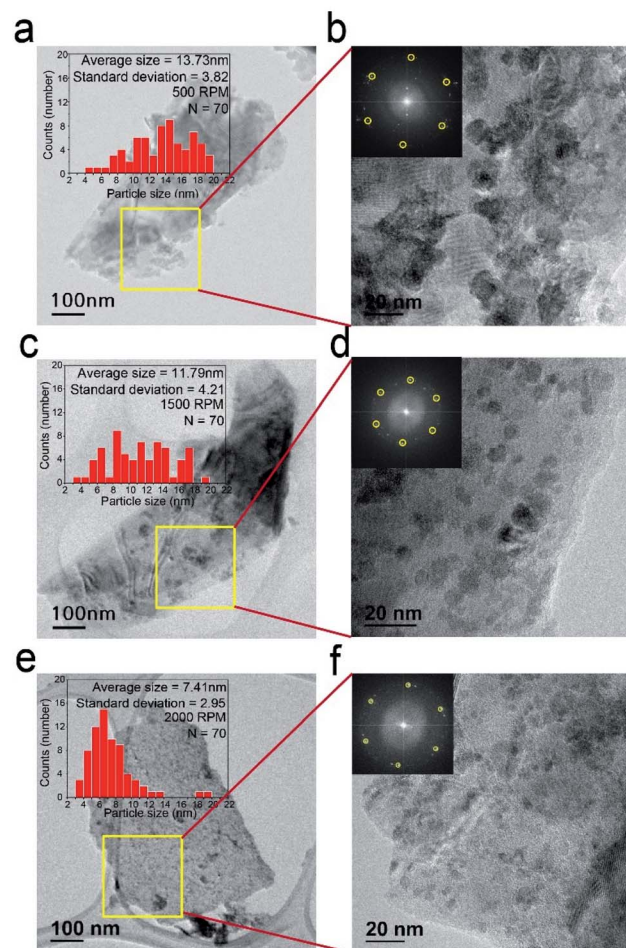


Fig. 3 Size distributions of  $\text{Fe}_2\text{O}_3$  nanoparticles and TEM images of  $\text{Fe}_2\text{O}_3@\text{MoS}_2$  nanocomposite synthesized at (a) 500 rpm, (c) 1500 rpm, and (e) 2000 rpm in the Taylor–Couette flow reactor, and their magnified TEM images with FFT diffraction patterns of  $\text{Fe}_2\text{O}_3@\text{MoS}_2$  nanocomposite synthesized at (b) 500 rpm, (d) 1500 rpm, and (f) 2000 rpm.

materials.<sup>24,25</sup> In order to compare the synthesis of  $\text{Fe}_2\text{O}_3$  nanoparticles at different rpm,  $\text{Fe}_2\text{O}_3@\text{MoS}_2$  nanocomposite was synthesized in the Taylor–Couette flow reactor at various rotation speeds of inner cylinder. Fig. 3a and b show  $\text{Fe}_2\text{O}_3@\text{MoS}_2$  nanocomposite synthesized at 500 rpm in the Taylor–Couette flow reactor. According to the TEM image and size distribution data,  $\text{Fe}_2\text{O}_3$  nanoparticles showed an average size of about  $13.73 \pm 3.82 \text{ nm}$ . As rpm increased, the average size of  $\text{Fe}_2\text{O}_3$  nanoparticles decreased to  $11.79 \pm 4.21 \text{ nm}$  at 1500 rpm of rotation speed (Fig. 3c and d). Uniformity of the  $\text{Fe}_2\text{O}_3$  nanoparticles was improved at 2000 rpm of rotation speed, and the average size of  $\text{Fe}_2\text{O}_3$  nanoparticles was also reduced to  $7.41 \pm 2.95 \text{ nm}$  (Fig. 3e and f).

Even in the top down method without heating,  $\text{Fe}_2\text{O}_3$  nanoparticles were distributed well on  $\text{MoS}_2$  nanosheets. Based on the TEM image, the size distribution of  $\text{Fe}_2\text{O}_3$  nanoparticles on  $\text{MoS}_2$  nanosheets was obtained, showing average size of the nanoparticles as 7.41 nm and mostly less than 10 nm at 2000 rpm of rotation speed.  $\text{Fe}_2\text{O}_3$  nanoparticles usually require



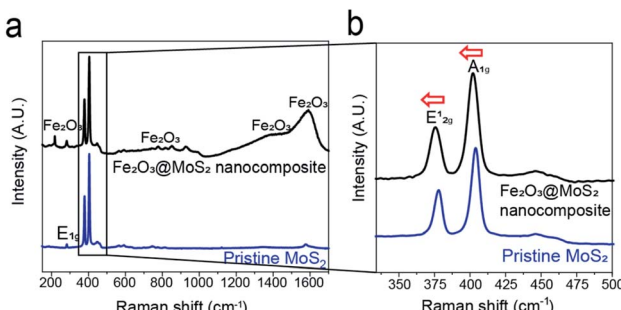


Fig. 4 (a) Raman spectroscopy data of pristine MoS<sub>2</sub> and Fe<sub>2</sub>O<sub>3</sub>@MoS<sub>2</sub> nanocomposite, (b) and its magnified data from 340 to 500 cm<sup>-1</sup>.

thermal treatment for their synthesis.<sup>13–15,17</sup> However, in our study, no thermal treatment was conducted. Increased mixing characteristics with increasing rpm of Taylor–Couette flow reactor<sup>46</sup> made Fe<sub>2</sub>O<sub>3</sub> nanoparticles synthesized on MoS<sub>2</sub> nanosheets in a nanometer scale without thermal treatment. In addition, TEM grid was observed below the transparent MoS<sub>2</sub> nanosheets, indicating adequate exfoliation of MoS<sub>2</sub>.

### Chemical composition and synthetic mechanism of Fe<sub>2</sub>O<sub>3</sub>@MoS<sub>2</sub> nanocomposite

Raman spectroscopy and XPS were used to examine the chemical state of Fe<sub>2</sub>O<sub>3</sub>@MoS<sub>2</sub> nanocomposite by measuring its response to photons. E<sub>2g</sub><sup>1</sup> mode reflects the in-plane vibration, and the A<sub>1g</sub> mode reflects the out-plane vibration of MoS<sub>2</sub>.<sup>48</sup> Fig. 4a shows the Raman spectroscopy data of Fe<sub>2</sub>O<sub>3</sub>@MoS<sub>2</sub> nanocomposite and pristine MoS<sub>2</sub>, and peaks for MoS<sub>2</sub> and Fe<sub>2</sub>O<sub>3</sub> were observed. In Fig. 4b, the E<sub>2g</sub><sup>1</sup> mode of Fe<sub>2</sub>O<sub>3</sub>@MoS<sub>2</sub> nanocomposite was located at 375.7 cm<sup>-1</sup>, while the E<sub>2g</sub><sup>1</sup> mode of pristine MoS<sub>2</sub> was located at 379.9 cm<sup>-1</sup>. Also the A<sub>1g</sub> mode of Fe<sub>2</sub>O<sub>3</sub>@MoS<sub>2</sub> nanocomposite was located at 401.4 cm<sup>-1</sup>, and A<sub>1g</sub> mode of pristine MoS<sub>2</sub> was located at 404.2 cm<sup>-1</sup>. A<sub>1g</sub> mode of Fe<sub>2</sub>O<sub>3</sub>@MoS<sub>2</sub> nanocomposite were shifted less than E<sub>2g</sub><sup>1</sup> mode. According to previous study, it means that out-plane of MoS<sub>2</sub> was affected by the external factor,<sup>47</sup> presumably Fe<sub>2</sub>O<sub>3</sub> nanoparticles, which are bonded to the basal plane (out-plane) of MoS<sub>2</sub>.

XPS analysis was performed to confirm the interaction, and chemical composition of Fe<sub>2</sub>O<sub>3</sub> nanoparticles and MoS<sub>2</sub> nanosheets.<sup>20,25,42</sup> Survey scan data show that both iron oxide and molybdenum disulfide exist in Fe<sub>2</sub>O<sub>3</sub>@MoS<sub>2</sub> nanocomposite (Fig. 5a). In Fig. 5b and c, Fe2p and O1s scan were used to compare the synthesis of Fe<sub>2</sub>O<sub>3</sub> nanoparticles on MoS<sub>2</sub> and other 2D substrates. Since FeCl<sub>3</sub> with Fe<sup>3+</sup> was used as the precursor, the Fe2p scan of all experimental groups shows the typical Fe<sup>3+</sup> and its satellite peaks at 710.7 eV, and 719.2 eV, respectively, which are similar to pristine Fe<sub>2</sub>O<sub>3</sub>.<sup>44</sup> O–Fe bond and O–H bond in O1s scan represent Fe<sub>2</sub>O<sub>3</sub> and Fe(OH)<sub>3</sub>, respectively, and the ratio between O–H bond and O–Fe bond depends on the kind of substrates. The ratio of O–Fe bond to O–H bond was 70 : 30 in Fe<sub>2</sub>O<sub>3</sub>@MoS<sub>2</sub> nanocomposite. On the other hand, the ratios of O–Fe bond to O–H bond were 46 : 54 and 37 : 63 in graphite and hBN, respectively, with the Fe<sup>3+</sup>

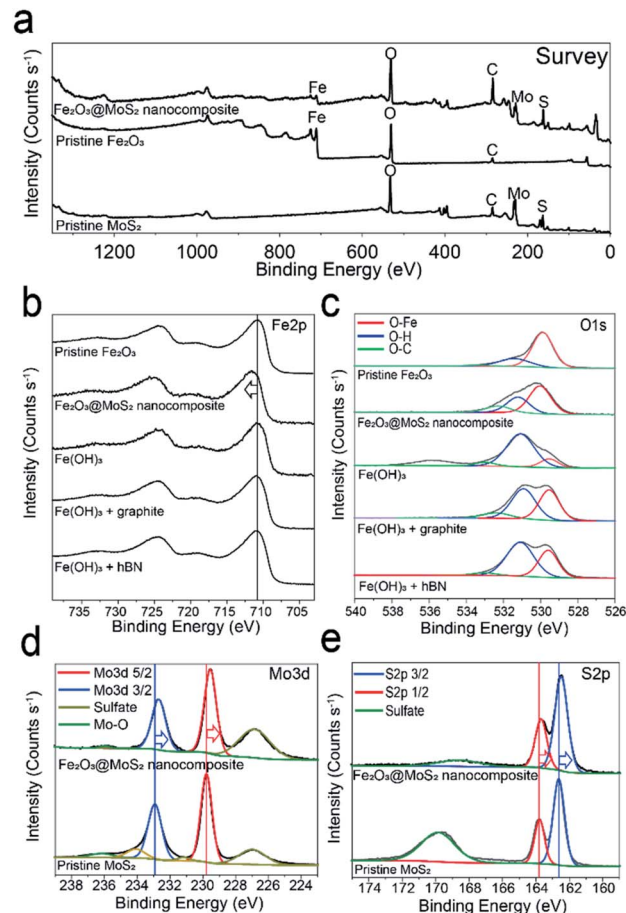


Fig. 5 XPS (a) survey scan of Fe<sub>2</sub>O<sub>3</sub>@MoS<sub>2</sub> nanocomposite, pristine Fe<sub>2</sub>O<sub>3</sub>, and pristine MoS<sub>2</sub>, (b) Fe2p and (c) O1s scan of pristine Fe<sub>2</sub>O<sub>3</sub>, Fe<sub>2</sub>O<sub>3</sub>@MoS<sub>2</sub> nanocomposite, and Fe(OH)<sub>3</sub> with various substrate reacted in the Taylor–Couette flow reactor, (d) Mo3d and (e) S2p scan of Fe<sub>2</sub>O<sub>3</sub>@MoS<sub>2</sub> nanocomposite and pristine MoS<sub>2</sub>.

precursor. The ratio of O–Fe bond to O–H bond was highest in Fe<sub>2</sub>O<sub>3</sub>@MoS<sub>2</sub> nanocomposite, and these results signify that, Fe<sub>2</sub>O<sub>3</sub> is converted successfully from FeCl<sub>3</sub> with NaOH on MoS<sub>2</sub> substrate better than on graphite or hBN in the Taylor–Couette flow reactor. Previous research has reported that the interface between Fe<sub>2</sub>O<sub>3</sub>, and MoS<sub>2</sub> has a lower formation energy of  $-1.76$  eV for chemical bonding.<sup>49,50</sup> To further confirm the chemical bonding between MoS<sub>2</sub> and Fe<sub>2</sub>O<sub>3</sub>, the binding energy of Fe<sub>2</sub>O<sub>3</sub>@MoS<sub>2</sub> nanocomposite was compared with the pristine Fe<sub>2</sub>O<sub>3</sub> and pristine MoS<sub>2</sub>. Fe2p scan data of Fe<sub>2</sub>O<sub>3</sub>@MoS<sub>2</sub> nanocomposite reveal the peak for Fe<sup>3+</sup> at 711.7 eV, red shifted by 1 eV compared to pristine Fe<sub>2</sub>O<sub>3</sub>. On the other hand, Mo3d and S2p scans of the Fe<sub>2</sub>O<sub>3</sub>@MoS<sub>2</sub> nanocomposite show 0.7 eV and 0.2 eV blue shifted binding energies, respectively, compared to pristine MoS<sub>2</sub> in Fig. 5d and e. The shifts of binding energy in Fe<sub>2</sub>O<sub>3</sub>@MoS<sub>2</sub> nanocomposite indicate a chemical interaction between Fe<sub>2</sub>O<sub>3</sub> nanoparticles and MoS<sub>2</sub> nanosheets as shown by Raman spectroscopy data. XPS and Raman spectroscopy data of Fe<sub>2</sub>O<sub>3</sub>@MoS<sub>2</sub> nanocomposite show that even in a fluid dynamic-based production method without heating, Fe<sub>2</sub>O<sub>3</sub> nanoparticles were bound to MoS<sub>2</sub> nanosheets



by chemical bonds, and  $\text{MoS}_2$  nanosheet is effective 2D substrates to incorporate  $\text{Fe}_2\text{O}_3$  nanoparticles.

In XPS analysis, atomic ratio of Fe and Mo was 3 : 6.6, which is similar to that of the precursor ratio of 3 : 7. Further compositional analysis was conducted by ICP-OES, which confirmed successful conversion of  $\text{FeCl}_3$  to  $\text{Fe}_2\text{O}_3$  nanoparticles. The ICP-OES data show atomic ratio of 3 : 6.3, which is almost identical to the atomic ratio between Fe and Mo in the XPS data (Table S1†).

### Glycolysis of PET by $\text{Fe}_2\text{O}_3@\text{MoS}_2$ nanocomposite

Because glycolysis reaction occurs at the temperature above 175 °C, it is necessary to confirm the thermal stability of  $\text{Fe}_2\text{O}_3@\text{MoS}_2$  nanocomposite. Fig. S5a and b† present the TGA data and derivative thermogravimetry (DTG) data, which showed no reduction below 400 °C. There was small increase of mass at 400 °C because of nitrogen adsorption followed by the reduction at high temperature. Since the glycolysis reaction was performed below 300 °C,  $\text{Fe}_2\text{O}_3@\text{MoS}_2$  nanocomposite will be thermally stable during the reaction.

Previously suggested mechanism of PET glycolysis using  $\text{Fe}_2\text{O}_3$  is shown in Fig. 6a.<sup>44,51</sup> The yield of BHET in PET glycolysis was measured by conventional method using HPLC,<sup>27</sup> and the comparison with previous reports is presented in Table S2.† Fig. 6b shows the conversion of PET with  $\text{Fe}_2\text{O}_3@\text{MoS}_2$  nanocomposite having various Fe : Mo ratios.  $\text{MoS}_2$  nanosheets show only 7% conversion in the glycolysis of PET, and the conversion of PET using  $\text{Fe}_2\text{O}_3@\text{MoS}_2$  nanocomposite was found to be saturated in the Fe : Mo ratio of 3 : 7. Fig. 6c shows the conversion of PET with the varying ratio between PET and  $\text{Fe}_2\text{O}_3@\text{MoS}_2$  nanocomposite. A 98% conversion of PET was reached at the ratio higher than 1/100. In Fig. 6d, the yield of BHET was maintained at around 90% up to 250 °C. However,

the yield of BHET suddenly decreased at 275 °C and continued to decrease to almost 50% at 300 °C. To analyze the decrease in yield, the process was carried out at 300 °C for 3 to 5 h (Fig. 6e) and showed further decrease in yield to 38%. Previous studies have reported that decreased yield of BHET in glycolysis of PET is caused by chemical equilibrium, and HPLC data of glycolysis product at 300 °C show by-product peaks in HPLC data different from HPLC data of commercial BHET and produced BHET at 225 °C (Fig. S6a–c†). There would be side reactions between BHET and EG or oligomer of PET, reducing the yield of BHET from 50% to less than 40% as reaction time increased.<sup>35</sup>

In Fig. S7a,†  $\text{Fe}_2\text{O}_3@\text{MoS}_2$  nanocomposite catalyst was recovered by simple filtration, and the recycling reaction with recycled catalyst was carried out at 225 °C for 3 h. During 7 recycles, the yield of BHET remained around 85% (Fig. 6f). TEM and ICP-OES were used to characterize the recovered  $\text{Fe}_2\text{O}_3@\text{MoS}_2$  nanocomposite. Fig. S7b and c† show the morphology of recovered  $\text{Fe}_2\text{O}_3@\text{MoS}_2$  nanocomposite. Even though  $\text{Fe}_2\text{O}_3@\text{MoS}_2$  nanocomposite was recycled repeatedly during PET glycolysis,  $\text{Fe}_2\text{O}_3$  nanoparticles are clearly distributed on  $\text{MoS}_2$  nanosheets in the recovered  $\text{Fe}_2\text{O}_3@\text{MoS}_2$  nanocomposite as fresh  $\text{Fe}_2\text{O}_3@\text{MoS}_2$  nanocomposite. ICP-OES data in Table S3† also show that the composition of Mo and Fe in recycled  $\text{Fe}_2\text{O}_3@\text{MoS}_2$  nanocomposite was maintained after the recycling. Although the catalytic yield and conversion rate are not superior to previous work, the production rate of  $\text{Fe}_2\text{O}_3@\text{MoS}_2$  nanocomposite was 1120 mg h<sup>-1</sup>, and is much higher than 0.2 mg h<sup>-1</sup> to 116.7 mg h<sup>-1</sup> of other reports and stable without decomposition or separation (Table S4†).

<sup>1</sup>H and <sup>13</sup>C NMR analyses were performed to confirm the purity of BHET as shown in Fig. 7a. NMR  $\delta$  values were as follows: white solid, <sup>1</sup>H NMR (DMSO-d<sub>6</sub>, 400 MHz,  $\delta$ /ppm),  $\delta$  = 8.09 (s, 4H),  $\delta$  = 4.95 (t, 2H),  $\delta$  = 4.28 (t, 4H),  $\delta$  = 3.69 (q, 4H). <sup>13</sup>C

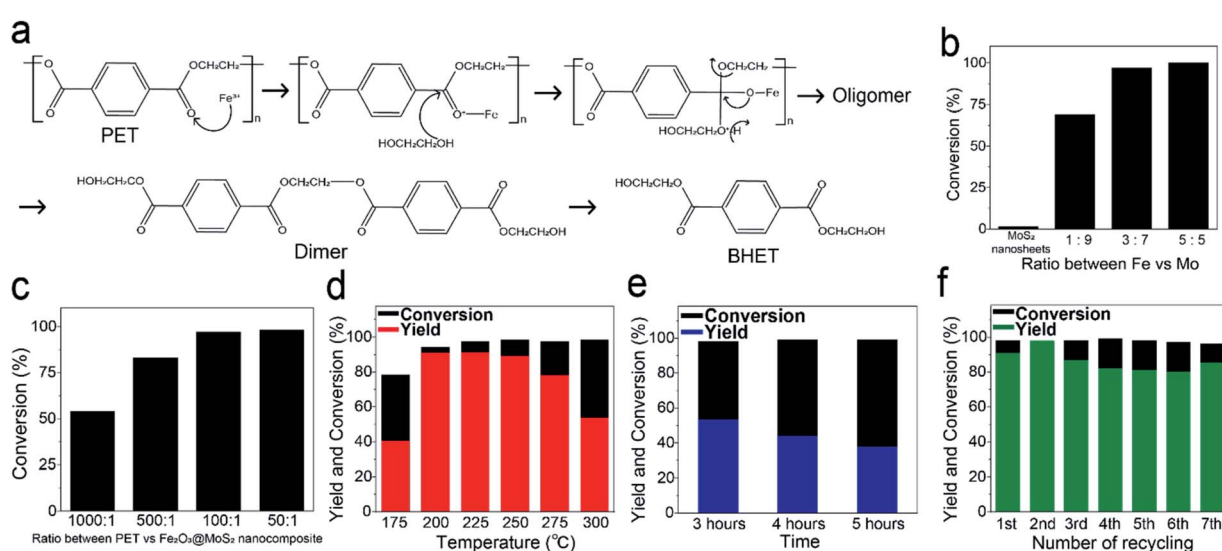


Fig. 6 (a) Suggested mechanism for glycolysis of PET using  $\text{Fe}_2\text{O}_3$  nanoparticles as a catalyst.<sup>44,51</sup> (b) conversion of PET with  $\text{MoS}_2$  nanosheets and various Fe : Mo ratio of  $\text{Fe}_2\text{O}_3@\text{MoS}_2$  nanocomposite, (c) conversion of PET with various ratio of PET and  $\text{Fe}_2\text{O}_3@\text{MoS}_2$  nanocomposite, yield and conversion (d) with 3 h reaction at different reaction temperature using  $\text{Fe}_2\text{O}_3@\text{MoS}_2$  nanocomposite, (e) at 300 °C with 3 different reaction time, and (f) with repeated recycling of catalyst at 225 °C for 3 h.



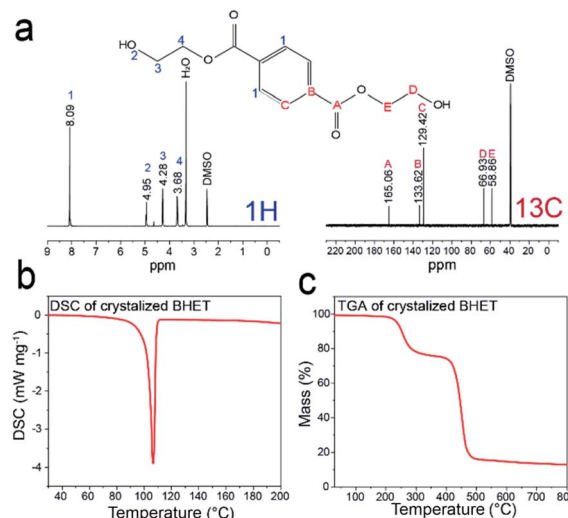


Fig. 7 (a) <sup>1</sup>H and <sup>13</sup>C NMR spectra data for produced BHET, (b) DSC data of crystallized BHET, (c) TGA data of crystallized BHET.

NMR (DMSO-d<sub>6</sub>, 400 MHz,  $\delta$ /ppm) data were:  $\delta$  = 165.06, 133.62, 129.42, 66.93, 58.86. Thus, the characteristic peaks of BHET consist of 5 carbons and 4 hydrogens indicated as A to E and 1 to 4 in NMR spectra data. Fig. 7b and c show DSC and TGA data of BHET. DSC curve shows a peak at 107 °C, and the TGA data show double decreases at 240 °C and 420 °C, showing the same thermal properties as reported previously for BHET.<sup>35,39</sup> Produced BHET is intended to be used as a monomer to synthesize polymeric material, and fewer impurity in BHET is more desirable. ICP-OES data indicating the residual amounts of Fe and Mo in the extracted BHET are shown in Table S5.† Only small amount of Fe and Mo, 10<sup>-4</sup> and 10<sup>-5</sup> weight percent, respectively, was detected in the extracted BHET.

In order to check whether the catalyst works effectively in the scaled-up process, the glycolysis reaction was performed with 100 g of PET. 100 g of PET was dispersed in 400 mL of EG with 1 g of Fe<sub>2</sub>O<sub>3</sub>@MoS<sub>2</sub> nanocomposite as shown in Fig. S8a.† The reaction was proceeded at 196 °C for 3 h with simple stirring under ambient condition. The product of glycolysis and produced BHET had identical brown and white color, respectively, with the previous product of glycolysis (Fig. S8b and c†), and HPLC data of product showed identical peaks with that of product from the smaller scale glycolysis of PET (Fig. S8d†). However, the peak of retention time at 18.37 is higher than that of commercial BHET (Fig. S6a†) which means higher contents of dimer. The yield and conversion were 87% and 94%, respectively. Therefore, Fe<sub>2</sub>O<sub>3</sub>@MoS<sub>2</sub> nanocomposite can be used in the increased scale of PET glycolysis and can be considered as an attractive catalyst in the recycling of large amount of PET by glycolysis to produce high quality BHET.

## Conclusions

We reported a method for the synthesis of uniform Fe<sub>2</sub>O<sub>3</sub> nanoparticles on exfoliated MoS<sub>2</sub> nanosheets due to the high mixing characteristics of the Taylor-Couette flow reactor.

Exfoliated MoS<sub>2</sub> nanosheets were produced in an aqueous solution with a thickness of few nanometers. Fe<sub>2</sub>O<sub>3</sub> nanoparticles were synthesized with a size below 7 nm without thermal or organic solvent treatment. Fe<sub>2</sub>O<sub>3</sub>@MoS<sub>2</sub> nanocomposite was synthesized at high production rate (1120 mg h<sup>-1</sup>) under mild conditions. Synthesized Fe<sub>2</sub>O<sub>3</sub>@MoS<sub>2</sub> nanocomposite was used for glycolysis of PET and showed an approximately 90% yield of high quality BHET. The aggregation of Fe<sub>2</sub>O<sub>3</sub> nanoparticles during the reaction was prevented by forming Fe<sub>2</sub>O<sub>3</sub> nanoparticles on MoS<sub>2</sub> nanosheets. Used Fe<sub>2</sub>O<sub>3</sub>@MoS<sub>2</sub> nanocomposite was recovered by simple filtration of glycolysis product without decomposition or separation of Fe<sub>2</sub>O<sub>3</sub> nanoparticles and MoS<sub>2</sub> nanosheets. Recovered Fe<sub>2</sub>O<sub>3</sub>@MoS<sub>2</sub> nanocomposite showed 94.4% catalytic activity of fresh Fe<sub>2</sub>O<sub>3</sub>@MoS<sub>2</sub> nanocomposite. Our method for the synthesis of Fe<sub>2</sub>O<sub>3</sub>@MoS<sub>2</sub> nanocomposite would be a promising strategy to produce large amount of catalyst necessary for large-scale catalytic processes.

## Conflicts of interest

There are no conflicts to declare.

## Acknowledgements

This work was supported by the National Research Foundation of Korea (NRF) grant funded by the Korea government (MSIT) (No. 2018R1A2A3075668) and the R&D Center for Valuable Recycling (Global-Top R&BD Program) of the Ministry of Environment (Project No. 2016002240001).

## Notes and references

- 1 A. Kumar and Q. Xu, *Chem. Nanostruct. Mater.*, 2018, **4**, 28–40.
- 2 R. I. Jafri, N. Rajalakshmi and S. Ramaprabhu, *J. Mater. Chem.*, 2010, **20**, 7114–7117.
- 3 X. Cai, Y. Luo, B. Liu and H.-M. Cheng, *Chem. Soc. Rev.*, 2018, **47**, 6224–6266.
- 4 Z. Fu, H. Zhang, C. Si, D. Legut, T. C. Germann, Q. Zhang, S. Du, J. S. Francisco and R. Zhang, *J. Phys. Chem. C*, 2018, **122**, 4710–4722.
- 5 H. Long, A. Harley-Trochimczyk, T. Pham, Z. Tang, T. Shi, A. Zettl, C. Carraro, M. A. Worsley and R. Maboudian, *Adv. Funct. Mater.*, 2016, **26**, 5158–5165.
- 6 Y.-C. Chen, A.-Y. Lu, P. Lu, X. Yang, C.-M. Jiang, M. Mariano, B. Kaehr, O. Lin, A. Taylor, I. D. Sharp, L.-J. Li, S. S. Chou and V. Tung, *Adv. Mater.*, 2017, **29**, 1703863.
- 7 N. Bandaru, R. S. Kumar, D. Snead, O. Tschauner, J. Baker, D. Antonio, S.-N. Luo, T. Hartmann, Y. Zhao and R. Venkat, *J. Phys. Chem. C*, 2014, **118**, 3230–3235.
- 8 L. Nurdwijayanto, R. Ma, N. Sakai and T. Sasaki, *Inorg. Chem.*, 2017, **56**, 7620–7623.
- 9 H. S. Sen, H. Sahin, F. M. Peeters and E. Durgun, *J. Appl. Phys.*, 2014, **116**, 083508.
- 10 S. Najmaei, A. Mlayah, A. Arbouet, C. Girard, J. Leotin and J. Lou, *ACS Nano*, 2014, **8**, 12682–12689.



11 Y. Cheng, S. Lu, F. Liao, L. Liu, Y. Li and M. Shao, *Adv. Funct. Mater.*, 2017, **27**, 1700359.

12 J. Hu, C. Zhang, Y. Zhang, B. Yang, Q. Qi, M. Sun, F. Zi, M. K. H. Leung and B. Huang, *Small*, 2020, **16**, 2002212.

13 M. B. Lejbini and P. Sangpour, *Optik*, 2019, **177**, 112–117.

14 X. Yang, H. Sun, L. Zhang, L. Zhao, J. Lian and Q. Jiang, *Sci. Rep.*, 2016, **6**, 31591.

15 C.-Y. Wu, W.-E. Chang, Y.-G. Sun, J.-M. Wu and J.-G. Duh, *Mater. Chem. Phys.*, 2018, **219**, 311–317.

16 Y. Chen, B. Song, X. Tang, L. Lu and J. Xue, *Small*, 2014, **10**, 1536–1543.

17 N. D. Chuong, T. D. Thanh, N. H. Kim and J. H. Lee, *ACS Appl. Mater. Interfaces*, 2018, **10**, 24523–24532.

18 T. Liu, S. Shi, C. Liang, S. Shen, L. Cheng, C. Wang, X. Song, S. Goel, T. E. Barnhart, W. Cai and Z. Liu, *ACS Nano*, 2015, **9**, 950–960.

19 Y. A. Kabachii, A. S. Golub, S. Y. Kochev, N. D. Lenenko, S. S. Abramchuk, M. Y. Antipin, P. M. Valetsky, B. D. Stein, W. E. Mahmoud, A. A. Al-Ghamdi and L. M. Bronstein, *Chem. Mater.*, 2013, **25**, 2434–2440.

20 V. Nandwana, W. Huang, Y. Li and V. P. Dravid, *ACS Appl. Nano Mater.*, 2018, **1**, 1949–1958.

21 A. S. K. Kumar, S.-J. Jiang and J. K. Warchol, *ACS Omega*, 2017, **2**, 6187–6200.

22 A. K. Yadav, M. J. Barandiaran and J. C. Cal, *Chem. Eng. J.*, 2012, **198–199**, 191–200.

23 A. Igder, S. Pye, A. H. M. Al-Antaki, A. Keshavarz, C. L. Raston and A. Nosrati, *RSC Adv.*, 2020, **10**, 14761–14767.

24 D. Seo, W.-S. Kim and D. H. Kim, *Chem. Eng. J.*, 2020, **399**, 125726.

25 J.-M. Jeong, H. G. Kang, H.-J. Kim, S. B. Hong, H. Jeon, S. Y. Hwang, D. Seo, B. E. Kwak, Y.-K. Han, B. G. Choi and D. H. Kim, *Adv. Funct. Mater.*, 2018, **28**, 1802952.

26 H. Jeon, J.-M. Jeong, H. G. Kang, H.-J. Kim, J. Park, D. H. Kim, Y. M. Jung, S. Y. Hwang, Y.-K. Han and B. G. Choi, *Adv. Energy Mater.*, 2018, **8**, 1800227.

27 J.-M. Jeong, S. B. Jin, H. J. Park, S. H. Park, H. Jeon, H. Suh, Y.-J. Park, D. Seo, S. Y. Hwang, D. H. Kim and B. G. Choi, *Adv. Mater. Interfaces*, 2020, **7**(16), 2000599.

28 X. Zhang, M. Fevre, G. O. Jones and R. M. Waymouth, *Chem. Rev.*, 2018, **118**, 839–885.

29 A. Rahimi and J. M. García, *Nat. Rev. Chem.*, 2017, **1**, 0046.

30 J. Zhang, X. Wang, J. Gong and Z. Gu, *J. Appl. Polym. Sci.*, 2004, **93**, 1089–1096.

31 F. Awaja and D. Pavel, *Eur. Polym. J.*, 2005, **41**, 1453–1477.

32 J. Chen, J. Lv, Y. Ji, J. Ding, X. Yang, M. Zou and L. Xing, *Polym. Degrad. Stab.*, 2014, **107**, 178–183.

33 S. R. Shukla and A. M. Harad, *Polym. Degrad. Stab.*, 2006, **91**, 1850–1854.

34 E. H. Acero, D. Ribitsch, G. Steinkellner, K. Gruber, K. Greimel, I. Eiteljorg, E. Trotscha, R. Wei, W. Zimmermann, M. Zinn, A. Cavaco-Paulo, G. Freddi, H. Schwab and G. Guebitz, *Macromolecules*, 2011, **44**, 4632–4640.

35 M. Imran, D. H. Kim, W. A. Al-Masry, A. Mahmood, A. Hassan, S. Haider and S. M. Ramay, *Polym. Degrad. Stab.*, 2013, **98**, 904–915.

36 A. B. Raheem, Z. Z. Noor, A. Hassan, M. K. A. Hamid, S. A. Samsudin and A. H. Sabeen, *J. Cleaner Prod.*, 2019, **225**, 1052–1064.

37 D. E. Nikles and M. S. Farahat, *Macromol. Mater. Eng.*, 2005, **290**, 13–30.

38 N. George and T. Kurian, *Ind. Eng. Chem. Res.*, 2014, **53**, 14185–14198.

39 A. M. Al-Sabagh, F. Z. Yehia, A. M. F. Eissa, M. E. Moustafa, G. Eshaq, A. M. Rabie and A. E. ElMetwally, *Polym. Degrad. Stab.*, 2014, **110**, 364–377.

40 A. M. Al-Sabagh, F. Z. Yehia, A.-M. M. F. Eissa, M. E. Moustafa, G. Eshaq, A.-R. M. Rabie and A. E. ElMetwally, *Ind. Eng. Chem. Res.*, 2014, **53**, 18443–18451.

41 M. Imran, K. G. Lee, Q. Imtiaz, B.-K. Kim, M. Han, B. G. Cho and D. H. Kim, *J. Nanosci. Nanotechnol.*, 2011, **11**, 824–828.

42 I. Cano, C. Martin, J. A. Fernandes, R. W. Lodge, J. Dupont, F. A. Casado-Carmona, R. Lucena, S. Cardenas, V. Sans and I. Pedro, *Appl. Catal., B*, 2020, **260**, 118110.

43 F. R. Veregué, C. T. P. Silva, M. P. Moisés, J. G. Meneguin, M. R. Guilherme, P. A. Arroyo, S. L. Favaro, E. Radovanovic, E. M. Girotto and A. W. Rinaldi, *ACS Sustainable Chem. Eng.*, 2018, **6**, 12017–12024.

44 L. Bartolome, M. Imran, K. G. Lee, A. Sangalang, J. K. Ahn and D. H. Kim, *Green Chem.*, 2014, **16**, 279–286.

45 G. Park, L. Bartolome, K. G. Lee, S. J. Lee, D. H. Kim and T. J. Park, *Nanoscale*, 2012, **4**, 3879–3885.

46 M. Nemri, S. Charton and E. Climent, *Chem. Eng. Sci.*, 2016, **139**, 109–124.

47 A. S. George, Z. Mutlu, R. Ionescu, R. J. Wu, J. S. Jeong, H. H. Bay, Y. Chai, K. A. Mkhoyan, M. Ozkan and C. S. Ozkan, *Adv. Funct. Mater.*, 2014, **24**, 7461–7466.

48 S. Wang, X. Wang and J. H. Warner, *ACS Nano*, 2015, **9**, 5246–5254.

49 H. Pan, X. Meng, X. Qi and G. Qin, *CrystEngComm*, 2017, **19**, 6333–6338.

50 Y. Zhao, W. Cai, Y. Shi, J. Tang, Y. Gong, M. Chen and Q. Zhong, *ACS Sustainable Chem. Eng.*, 2020, **8**, 12603–12611.

51 A. M. Al-Sabagh, F. Z. Yehia, D. R. K. Harding, G. Eshaq and A. E. ElMetwally, *Green Chem.*, 2016, **18**, 3997–4003.

